International Journal of Energy Research

WILEY

RESEARCH ARTICLE OPEN ACCESS

Efficient Porous-Medium Framework for Compact Heat Pipe Heat Exchanger

Seungjae Lee[1] | Jin Hyeuk Seo[2] | Yunseo Kim[3] | Hoon Choi[1] | Seong Hyuk Lee[1] | Jungho Lee[2] | Hyoungsoon Lee[1]

[1]School of Mechanical Engineering, Chung-Ang University, 84, Heukseok-ro, Dongjak-gu, Seoul 06974, Republic of Korea | [2]Department of Mechanical Engineering, Ajou University, 206, Worldcup-ro, Yeongtong-gu, Suwon 16499, Gyeonggi-do, Republic of Korea | [3]Department of Mechanical Engineering, University of Maryland, College Park 20742, Maryland, USA

Correspondence: Jungho Lee (jungholee@ajou.ac.kr) | Hyoungsoon Lee (leeh@cau.ac.kr)

Received: 23 October 2025 | **Revised:** 28 February 2026 | **Accepted:** 5 March 2026

Academic Editor: Akshay Kumar Saha

Keywords: compact heat pipe heat exchanger | porous-medium modeling | thermal–hydraulic performance | waste heat recovery

ABSTRACT

Waste heat recovery is one of the most effective strategies for improving global energy efficiency. However, accurately modeling of compact heat pipe heat exchangers (HPHXs) remains computationally challenging due to their intricate fin geometries and complex phase-change processes. This work introduces a porous-medium modeling framework that combines anisotropic flow resistance coefficients with a local thermal nonequilibrium (LTNE) formulation. The approach enables precise resolution of thermal gradients and interfacial heat transfer while significantly reducing computational costs. Experimental validation was conducted on a representative compact HPHX and benchmarked against both a conventional local thermal equilibrium (LTE) porous-medium model and a fully resolved fin-geometry simulation. The LTNE model predicted heat transfer and pressure drop with errors within 5%, while reducing hot- and cold-side pressure drop errors by ~45% and 60%, respectively, compared to LTE. It also eliminated the systematic overprediction of heat transfer observed in LTE. Matching the accuracy of the fully resolved fin model, the LTNE framework achieved a ~97% reduction in computational time, offering an accurate and efficient alternative for large-scale simulations. These results establish the anisotropic-LTNE porous-medium framework as a robust and scalable tool for the design and optimization of next-generation compact heat recovery systems.

1 | Introduction

Global energy demand continues to rise with rapid industrialization, reinforcing dependence on fossil fuels, and accelerating greenhouse gas emissions [1, 2]. According to the analysis, ~72% of global primary energy is dissipated during energy conversion processes. In particular, about 63% of the identified waste heat sources occur at temperatures below 100°C [3]. When effectively recovered, this waste heat, emitted from industrial processes, power generation, and mechanical equipment, offers substantial potential for energy conservation and emission reduction.

Compact heat pipe heat exchangers (HPHXs) have emerged as a pivotal technology for waste heat recovery, offering high efficiency and operational reliability [4, 5]. Historically, the development of HPHX technology gained momentum in the late 1990s and early 2000s, focusing on humidity control in HVAC systems and specialized hospital environments [6–8]. From the 2010s onward, HPHX applications broadened from building HVAC optimization to industrial waste heat recovery, including steel and ceramics industries [9–11].

Research has increasingly focused on enhancing the reliability and thermal performance of heat-pipe-based systems for high-power and extreme-environment applications. Advances in multiphysics modeling and system-level evaluation of heat-pipe-cooled reactors have demonstrated the importance of robust heat pipe designs [12, 13], while experimental studies have explored performance improvements in fin-assisted configurations [14]. Concurrently, entropy-generation analyses have been applied to complex heat exchanger geometries to reduce thermodynamic irreversibility [15]. These efforts have also contributed to refined thermal design and performance-analysis frameworks specifically for HPHXs [16]. In parallel, recent reviews have summarized key experimental developments in heat pipes for microreactor applications [17].

Despite their broad application, accurately predicting the thermal–hydraulic performance of HPHXs remains challenging. High-fidelity computational fluid dynamics (CFD) simulations that resolve complex fin geometries and multiphase heat transfer require extremely fine meshes, which drastically increase computational cost and analysis time [18, 19]. To manage this burden, simulations often reduce mesh resolution, but this inevitably compromises accuracy and reliability. To address these challenges, prior studies have explored simplified approaches, such as approximating heat pipes as solid rods [20] and exploiting geometric periodicity [21]. However, such structural simplifications often compromise predictive accuracy and fail to capture the detailed thermal–hydraulic behavior associated with complex fin and pin-fin geometries commonly encountered in compact heat exchangers [22].

Porous-medium modeling offers a powerful alternative by replacing detailed fin geometries with equivalent porous domains characterized by flow resistance and heat transfer coefficients (HTCs). Wang et al. [23], for example, applied this method to plate-fin heat exchangers using empirically derived resistance parameters. Many porous-medium studies adopt the local thermal equilibrium (LTE) assumption [24]. However, this assumption can introduce significant errors when large temperature gradients exist between the fluid and solid phases. Local thermal nonequilibrium (LTNE)-based models have been shown to reduce predictive uncertainty in various heat exchanger configurations [25, 26]. However, most LTNE studies assume isotropic resistance, overlooking the inherently anisotropic characteristics of finned structures. Furthermore, systematic comparisons among detailed fin-geometry CFD simulations, LTE porous-medium models, and anisotropic LTNE porous-medium models remain scarce, especially those supported by comprehensive experimental validation.

This study introduces an anisotropic-LTNE porous-medium modeling framework specifically developed for compact HPHXs. The framework incorporates anisotropic flow resistance coefficients and experimentally determined HTCs to capture local thermal gradients and interfacial exchange more accurately. Predictions from the proposed framework, a conventional LTE porous-medium model, and a fully resolved fin-geometry CFD model are validated against experimental data from a representative compact HPHX module under a range of operating conditions. Comparative analyses demonstrate that the proposed LTNE framework achieves near-benchmark accuracy while reducing computational time by more than 97%. These results establish the framework as a robust and scalable tool for the design and optimization of next-generation compact heat recovery systems.

2 | Experimental Method

An experimental campaign was conducted to validate the numerical models and to provide high-quality reference data for the thermal–hydraulic optimization of a compact HPHX. The work comprised the design and fabrication of a representative HPHX module, the construction of a dedicated test facility, and systematic tests under controlled operating conditions. This section describes the module fabrication; the experimental setup and operating parameters; the measurement procedures; and the associated uncertainty analysis.

2.1 | Design and Fabrication of the Compact HPHXH Test Module

A compact HPHX test module was designed and constructed to investigate thermal–hydraulic performance and to validate the numerical modeling approaches. As shown in Figure 1a, the assembled module had overall dimensions of 185 mm × 60 mm × 116 mm ($W \times L \times H$), with clearly defined inlet and outlet cross sections of 60 mm × 60 mm for the hot side and 60 mm × 50 mm for the cold side. To suppress parasitic heat conduction and ensure reliable thermal measurements, a 6-mm-thick polyetheretherketone (PEEK; thermal conductivity = 0.25 $W \cdot m^{-1} \cdot K^{-1}$) separator was installed between the two flow passages.

Figure 1b illustrates the finned heat-pipe components used in the module. Each of the nine heat pipes had an outer diameter of 9.52 mm and was equipped with 38 circular copper fins, each 0.5 mm thick, 6.24 mm high, and spaced 2.5 mm apart. Heat pipes were fabricated following a standard manufacturing process [27]. Each pipe was first evacuated with a rotary pump to below 10^{-5} Torr. Thoroughly degassed distilled water was then charged as the working fluid at a filling ratio of 50% of the internal hot-side volume. A minimum 1-h degassing step was performed to remove noncondensable gases, thereby reducing thermal resistance and improving operational reliability [28, 29]. After filling, the uppermost 10 mm of each pipe was hermetically sealed via ultrasonic welding to provide robust, airtight joints without introducing appreciable thermal resistance. The mass of each fabricated pipe was measured to confirm the correct filling ratio.

As presented in Figure 1c, the complete experimental facility consisted of the HPHX module, an airflow control system, and measurement instrumentation. The facility was designed to provide stable and repeatable operating conditions, enabling accurate measurements of the heat-transfer rate, effectiveness, and pressure drop across a wide range of test scenarios.

2.2 | Experimental Facility and Test Conditions for Thermal–Hydraulic Characterization

Figure 2 presents a schematic of the experimental facility and the data-acquisition (DAQ) system used for the thermal–hydraulic characterization of the compact HPHX. Airflow to the hot and cold sides was supplied by a blower (Dongkun Industrial Co., DTB-404) to provide stable, controllable operating conditions.

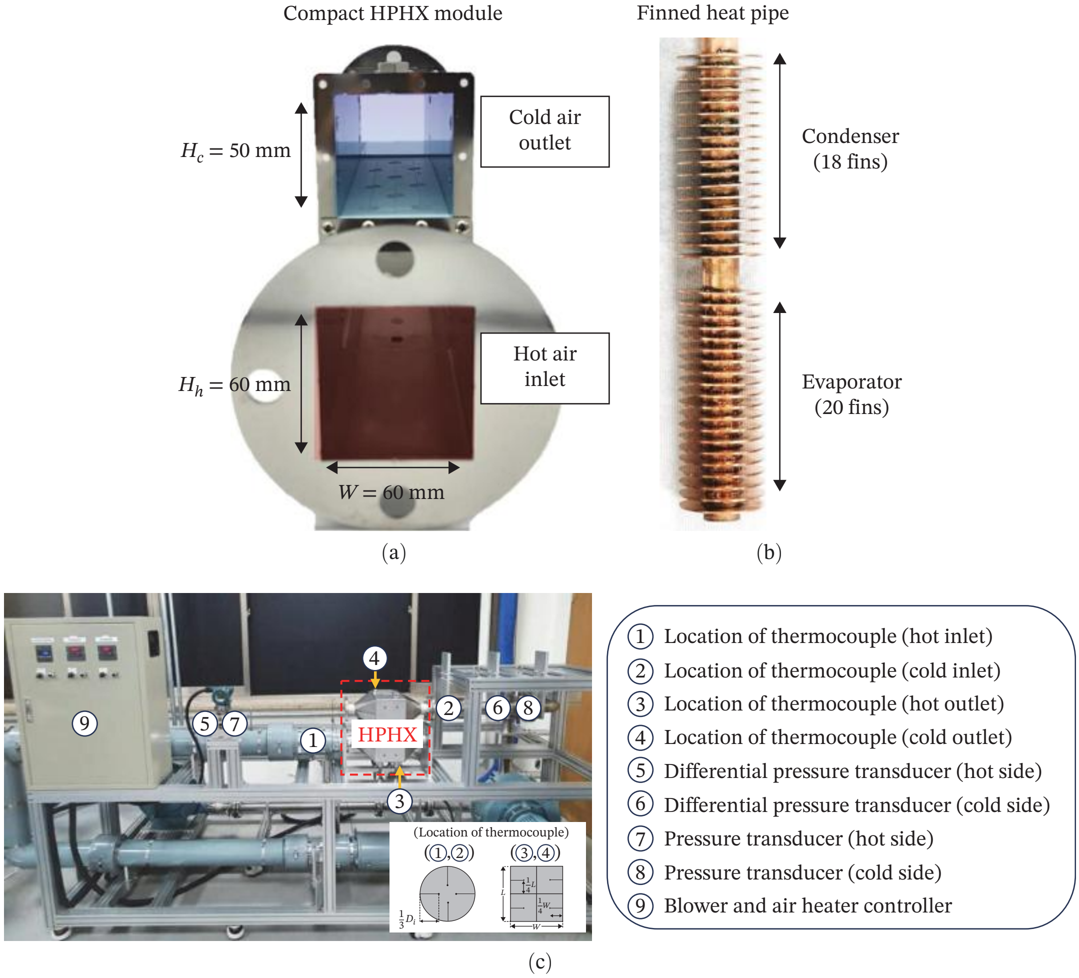

FIGURE 1 | Compact HPHX module and experimental setup. (a) Assembled compact HPHX module (185 mm × 60 mm × 116 mm) with separate hot- and cold-side inlet/outlet sections and a PEEK separator to suppress heat leakage. (b) Components of the finned heat pipes, including the copper fins and heat-pipe body. (c) Experimental facility comprising the HPHX module, airflow control system, and instrumentation for controlled testing and thermal–hydraulic performance measurements.

Mass flow rates were determined from the differential pressure measured across an ISO 5167-2 orifice plate using a differential-pressure transmitter (Yokogawa EJA110A). Static pressures upstream and downstream of the test section were monitored continuously with high-precision pressure transducers (Omega PX409; accuracy ±0.25% of full scale), and pressure-drop measurements were verified at dedicated ports using a high-resolution micro-manometer (Furness Controls FCO560; accuracy ±1 Pa).

On the hot side, an electric air heater (LEISTER LE 10000 DF-C; maximum output 5.5 kW) was installed upstream of the blower to regulate the inlet temperature. A high-shear static mixer was positioned downstream of the heater to ensure a uniform temperature distribution. On the cold side, inlet air temperature was maintained at 24°C by the laboratory's air-conditioning system.

Temperature measurements were acquired at six locations each at the inlet and outlet (12 locations total) using 24 calibrated T-type thermocouples (accuracy ±0.2°C). Pressure drops across the HPHX were measured through dedicated ports at the module inlet and outlet using the micro-manometer mentioned above. All experimental signals were recorded continuously by a VTI EX1032A DAQ system and logged with LabVIEW software for real-time monitoring and subsequent postprocessing.

2.3 | Experimental Test Procedure and Data Reduction

The experimental procedure began with establishing the desired airflow conditions. On the cold side, the airflow rate was fixed at 0.04 kg·s^{-1}, and the inlet temperature was maintained at 24°C using an air blower in combination with the laboratory's air-conditioning system. On the hot side, the airflow rate was set to 0.03, 0.04, or 0.05 kg·s^{-1}, while the inlet temperature was adjusted to 50, 75, 100, or 125°C using an electric air heater.

Steady-state operation was defined as a variation in the heat transfer rate within ±2% sustained over a continuous 10-min interval. Once steady-state was achieved, temperature and pressure data were recorded at 1-s intervals for 10 min, yielding 600 data points per condition. These data were used to calculate heat

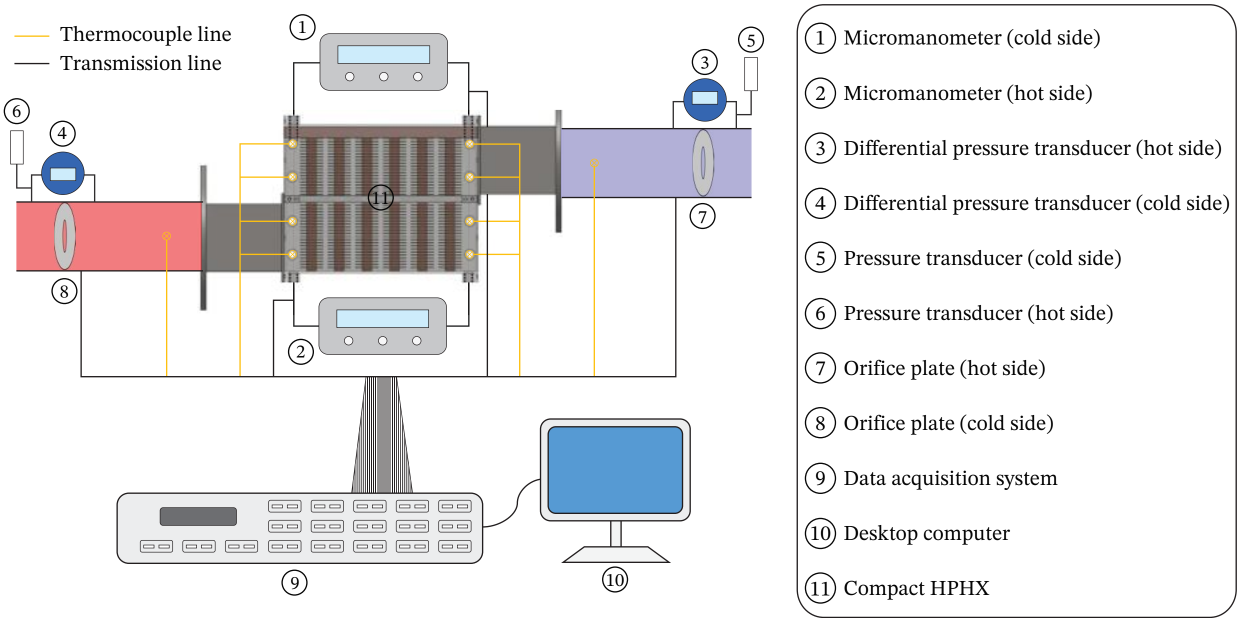

FIGURE 2 | Experimental facility and data acquisition system. Schematic of the test setup used for thermal–hydraulic characterization of the compact HPHX. Airflow rates, temperatures, and pressures were monitored in real time at the module inlet and outlet and recorded using a VTI EX1032A data-acquisition system integrated with LabVIEW.

transfer rates, effectiveness, and pressure drops. Table 1 summarizes the operating conditions.

The hot- and cold-side heat transfer rates were calculated as:

$$Q_h = \dot{m}_h c_{p,h} \left(T_{h,\text{in}} - T_{h,\text{out}} \right), \tag{1}$$

$$Q_c = \dot{m}_c c_{p,c} \left(T_{c,\text{out}} - T_{c,\text{in}} \right), \tag{2}$$

TABLE 1 | Summary of experimental operating conditions for the compact HPHX module.

	Hot-side inlet		Cold-side inlet	
Case	Mass flow rate ($kg \cdot s^{-1}$)	Temperature (°C)	Mass flow rate ($kg \cdot s^{-1}$)	Temperature (°C)
1	0.03	50	0.04	24
	0.04	50		
	0.05	50		
2	0.03	75		
	0.04	75		
	0.05	75		
3	0.03	100		
	0.04	100		
	0.05	100		
4	0.03	125		
	0.04	125		

where $\dot{m}$ is the mass flow rate and c_p is the specific heat capacity. Subscripts h, c, in, and out denote the hot side, the cold side, the inlet, and the outlet, respectively. Inlet and outlet temperatures ($T_{h,\text{in}}$, $T_{h,\text{out}}$, $T_{c,\text{in}}$, and $T_{c,\text{out}}$) were obtained by averaging multiple measurement points to ensure accurate thermal characterization.

The heat capacity rates of the hot and cold air streams were defined as:

$$C_h = \dot{m}_h c_{p,h}, \tag{3}$$

$$C_c = \dot{m}_c c_{p,c}, \tag{4}$$

The effectiveness (ε) of the HPHX was determined as the ratio of the actual heat transfer rate Q to the theoretical maximum heat transfer rate $Q_{\max}$:

$$\varepsilon = \frac{Q}{Q_{\max}}, \tag{5}$$

where $Q_{\max}$ was computed using the minimum heat capacity rate $C_{\min}$ and the inlet temperature difference:

$$Q_{\max} = C_{\min} \left(T_{h,\text{in}} - T_{c,\text{in}} \right). \tag{6}$$

Here, $C_{\min}$ is the smaller of C_h and C_c.

2.4 | Uncertainty Analysis

Experimental uncertainties associated with the heat transfer rate Q and effectiveness ε were evaluated following the *Guide to the Expression of Uncertainty in Measurement (GUM)* [30]. Individual uncertainties were quantified using a sensitivity-coefficient approach, as expressed in Equations (7) and (8).

$$\delta Q = \sqrt{\sum_{i=1}^{n} \left(\frac{\delta Q}{\delta x_i} \delta x_i \right)^2}, \tag{7}$$

$$\delta \varepsilon = \sqrt{\sum_{i=1}^{n} \left(\frac{\delta \varepsilon}{\delta x_i} \delta x_i \right)^2}, \tag{8}$$

where $\partial Q/\partial x_i$ and $\partial \varepsilon/\partial x_i$ represent sensitivity coefficients, and δx_i denotes the standard uncertainty of each measured variable. A coverage factor of 1.96 was applied to achieve a 95% confidence level. The average relative expanded uncertainties of ε and Q were 3.55% and 6.26%, respectively. Further details are provided in Table S1 and Section I of the Supporting Information.

3 | Numerical Model

A conjugate heat transfer numerical model was developed to evaluate and compare alternative modeling strategies for predicting the thermal–hydraulic performance of the compact HPHX. To reduce the computational burden of explicitly resolving intricate fin geometries, a porous-medium framework was established. In this approach, finned regions are represented as equivalent porous domains, enabling significant computational efficiency while maintaining predictive accuracy through anisotropically derived flow resistance and HTCs. Both LTE and LTNE formulations were implemented within this framework and comparatively analyzed to assess their predictive capability. In addition, a detailed CFD model explicitly resolving the fin structures was performed as a benchmark, allowing a rigorous evaluation of both predictive accuracy and computational efficiency of the porous-medium approaches.

3.1 | Conjugate Numerical Simulation of the Full-Scale Model

A detailed conjugate heat transfer CFD simulation of the full-scale compact HPHX was conducted to provide a benchmark for model validation. Figure 3 illustrates the computational domain and boundary conditions, configured to replicate the experimental geometry. Based on previous studies [31], a simplified model for the phase-change phenomena was achieved by representing the heat pipes as solid rods with an effective thermal conductivity of $k_{\mathrm{eff}} = 65{,}000\ \mathrm{W{\cdot}m^{-1}{\cdot}K^{-1}}$. The geometry included 20 fins on the hot side and 18 fins on the cold side, with nine heat pipes arranged in a staggered configuration across six rows.

Steady-state, incompressible flow was assumed. The SIMPLE algorithm was employed for pressure–velocity coupling due to its stability in conjugate heat transfer simulations. Gradient reconstruction was performed using a least-squares method, and second-order upwind discretization was applied for the pressure, momentum, and energy equations to enhance numerical accuracy and stability.

The realizable k–ε turbulence model was selected owing to its robustness in predicting turbulent heat transfer under high-Reynolds-number conditions with strong pressure gradients.

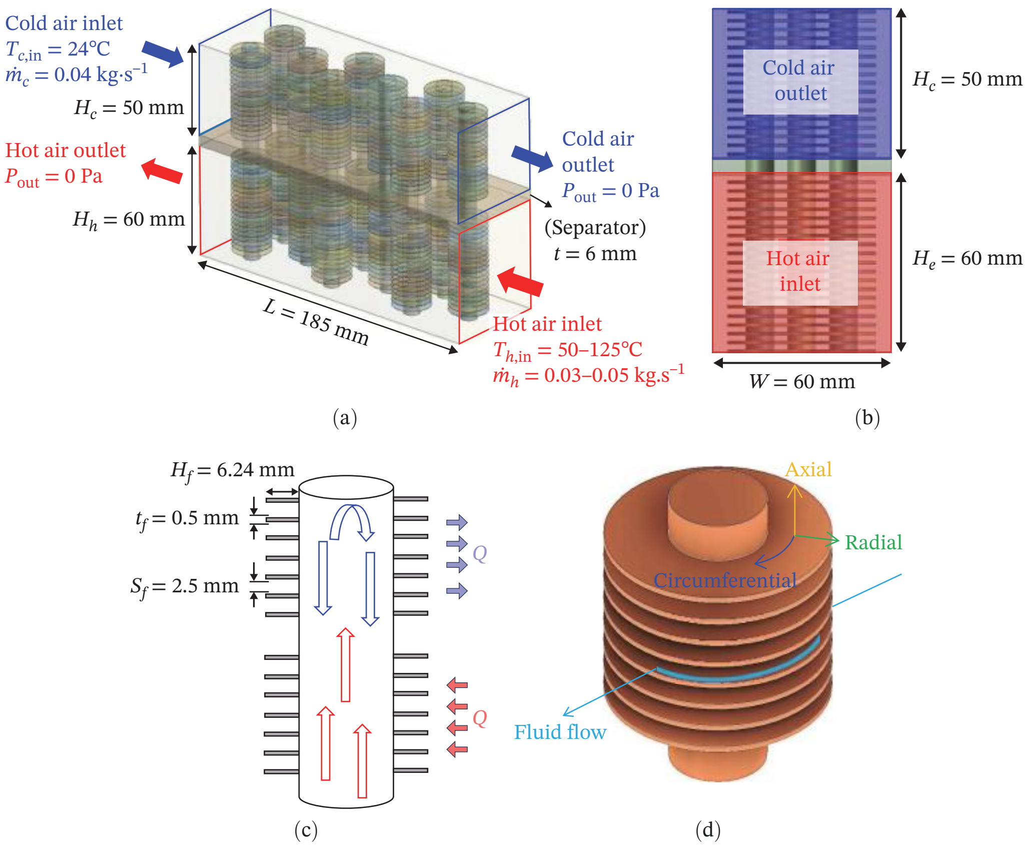

FIGURE 3 | Computational domain and boundary conditions of the compact HPHX. (a) Domain with applied boundary conditions. (b) Hot-side inlet and cold-side outlet regions. (c) Representation of heat transfer pathways. (d) Partial-fin configuration with associated fluid flow paths. The domain was constructed for steady-state conjugate heat transfer simulations, replicating the experimental geometry and operating conditions.

Convergence of the solution was considered to be achieved when the residuals for continuity, velocity components, turbulent kinetic energy (k), and dissipation rate (ε) dropped below 10^{-3}, while the residual for the energy equation fell below 10^{-6}.

Boundary conditions at the hot-side inlet were specified by mass flow rates with inlet temperatures ranging from 50 to 125°C, while the cold-side inlet temperature was fixed at 24°C. Pressure outlet conditions were applied at both hot- and cold-side exits. No-slip and conjugate heat transfer boundary conditions were imposed at all fluid–solid interfaces, and external surfaces were treated as adiabatic.

The computational domain was discretized using polyhedral elements with boundary-layer inflation (10 prism layers, growth ratio 1.2) to accurately capture near-wall transport phenomena. A mesh-independence study for the porous-medium models confirmed that variations in predicted Q were below 1% for meshes exceeding 8.8 million cells, validating the mesh resolution. In contrast, the explicitly resolved fin model required ~144 million elements to achieve practical convergence. Further details on the governing equations and mesh-independence analysis are provided in Sections II and III of the Supporting Information.

3.2 | Porous-Medium Modeling Framework

A porous-medium modeling framework was developed to represent the finned regions surrounding the heat pipes, substantially reducing computational complexity while maintaining predictive accuracy. As illustrated in Figure 4a, porous domains were applied over 54 mm of the 60 mm hot-side length and 48 mm of the 50 mm cold-side length. These dimensions were determined through sensitivity analyses to ensure complete coverage of the heat transfer region. The porous-medium model was constructed in two steps as follows: (i) anisotropic flow resistance coefficients were derived to capture directional flow behavior, and (ii) representative HTCs were quantified to enable accurate thermal predictions.

Flow resistance within the porous domain was modeled by introducing an additional momentum source term (S_i) into the momentum equations, expressed in tensor form as follows:

$$S_i = -\left(\sum_{j=1}^{3} D_{ij}\mu u_j + \sum_{j=1}^{3} C_{ij}\frac{1}{2}\rho|u|u_j\right), \tag{9}$$

where D_{ij} and C_{ij} denote the viscous and inertial resistance coefficients, respectively, which together account for the anisotropic flow resistance caused by the fin array. For a homogeneous porous medium, $D_{ij} = \mu/\alpha$, and $C_{ij} = C_2$, where μ is the dynamic viscosity, α is the permeability, and C_2 is the inertial resistance coefficient. Consequently, the momentum source term reduces to the following:

$$S_i = -\left(\frac{\mu}{\alpha}u_i + C_2\frac{1}{2}\rho|u|u_i\right) = -\left(C_1\mu u_i + C_2\frac{1}{2}\rho|u|u_i\right), \tag{10}$$

where α is the permeability, C_1 is the viscous resistance coefficient (α^{-1}), and ρ is the fluid density. Subsequently, the pressure drop (ΔP) for both the hot and cold sections was determined by performing unit-cell simulations over an air inlet velocity range of 1–10 m·s^{-1} in both the hot and cold sections. The correlation between ΔP and velocity (u) is given by [32] the following:

$$\Delta P = -S_i\Delta n = au^2 + bu, \tag{11}$$

with resistance coefficients related to the fitting parameters by the following:

$$a = \frac{1}{2}C_2\rho\Delta n, \tag{12}$$

$$b = C_1\mu\Delta n. \tag{13}$$

Resistance coefficients were determined from simulations of a circumferential unit-cell geometry representative of the finned structure. The resulting pressure drops were normalized by the corresponding porous thickness in each flow direction to account for anisotropic behavior. Thicknesses of 29.9 mm (circumferential flow), 6.25 mm (radial flow), and 0.5 mm (axial flow) were applied, yielding progressively larger resistance coefficients. The computed values are summarized in Table 2.

HTCs for the LTNE model were obtained from CFD simulations of representative fin–tube unit cells under operating mass flow rates of 0.03–0.05 kg·s^{-1}. These boundary conditions allowed for the accurate quantification of the HTCs. Unlike the LTE assumption of instantaneous thermal equilibrium, the LTNE formulation accounts for finite interfacial heat transfer, thereby improving prediction accuracy. Calculated HTCs are summa-

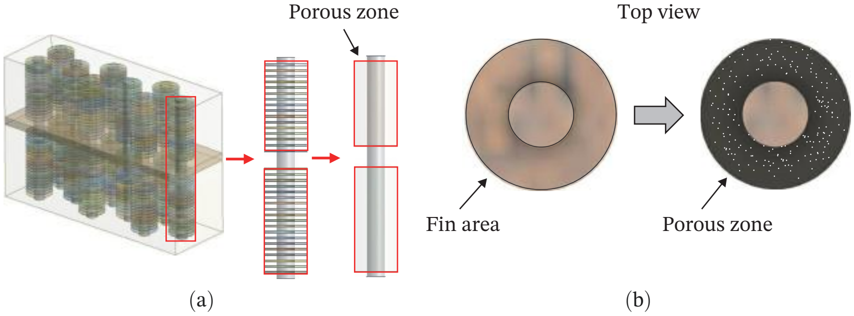

FIGURE 4 | Porous-medium representation of the finned tube. (a) Three-dimensional view of the finned tubes and corresponding porous regions. (b) Top view of the porous region. The porous-medium configuration reduces computational cost while preserving anisotropic flow resistance and heat transfer characteristics.

TABLE 2 | Viscous and inertial resistance coefficients of the anisotropic porous medium.

Direction	Viscous resistance coefficient (m^{-2})	Inertial resistance coefficient (m^{-1})
Circumferential	7.5×10^7	43
Radial	1×10^8	59
Axial	4.2×10^8	597

rized in Table 3. Further details of the computational methodology are provided in Section IV of the Supporting Information.

By integrating anisotropic resistance coefficients with representative HTCs, the porous-medium framework reproduces the complex thermal–fluid behavior of finned heat exchangers while substantially reducing computational cost and preserving predictive accuracy.

4 | Results and Discussion

This section presents the baseline thermal–hydraulic performance of the compact HPHX measured experimentally, as shown in Figure 5, and evaluates three numerical modeling approaches: the LTE porous-medium model, the LTNE porous-medium model, and a fully resolved fin CFD model. Model accuracy is assessed by direct comparison with experimental measurements of heat transfer rate, effectiveness, and pressure drop across the operating range, while computational efficiency is evaluated in terms of mesh requirements and convergence time. Due to the

TABLE 3 | Calculated heat transfer at different mass flow rates.

Hot inlet mass flow rate ($kg \cdot s^{-1}$)	HTC ($W \cdot m^{-2} \cdot K^{-1}$)	Cold inlet mass flow rate ($kg \cdot s^{-1}$)	HTC ($W \cdot m^{-2} \cdot K^{-1}$)
0.03	392	0.04	497
0.04	523		
0.05	653		

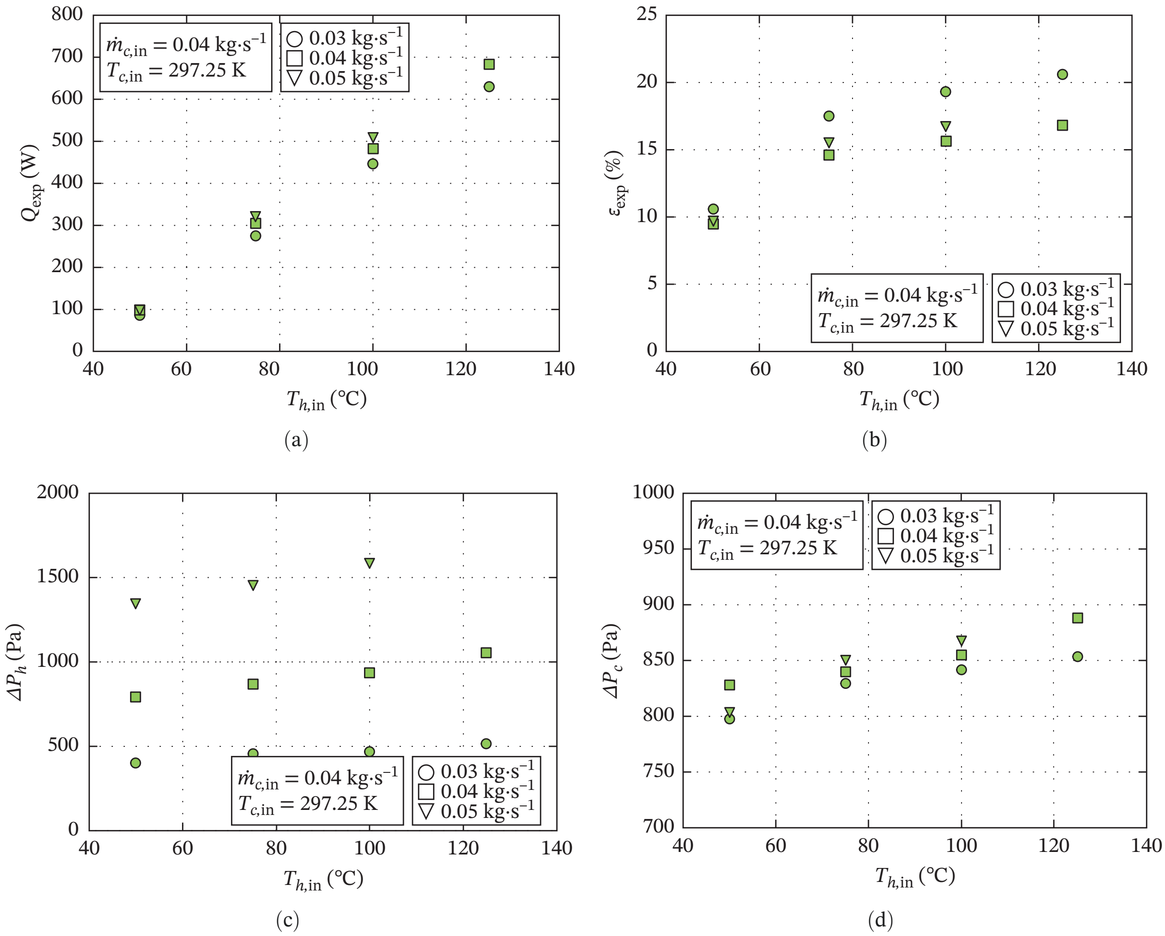

FIGURE 5 | Experimental thermal–hydraulic performance of the compact HPHX. (a) Heat transfer rate. (b) Effectiveness. (c) Hot-side pressure drop. (d) Cold-side pressure drop. These measurements provide baseline data for validating numerical predictions across a wide range of operating conditions.

extreme computational demands of achieving a fully mesh-converged solution for the fin-resolved model, Figures 6–8 focus on the porous-medium results for the complete set of operating conditions. Figure 9 provides a comparison of all three models for a representative case using high-resolution meshes, serving as a benchmark for predictive accuracy and clearly illustrating the trade-off between computational cost and solution fidelity through a mesh-refinement study.

4.1 | Experimental Characterization

Figure 5 summarizes the measured thermal–hydraulic performance of the compact HPHX. The heat transfer rate, shown in Figure 5a, increased nearly linearly with both hot-side mass flow rate and inlet temperature, reaching 683.3 W at 0.05 kg·s^{-1} and 125°C. At a fixed inlet temperature, increasing the mass flow rate from 0.03 to 0.05 kg·s^{-1} resulted in an average increase of ~35%. At a fixed mass flow rate, raising the inlet temperature from 50 to 125°C enhanced the heat transfer rate by nearly 290%. These increases reflect the combined effects of higher convective HTCs and larger temperature differences, both of which reduce the overall thermal resistance.

Effectiveness trends, presented in Figure 5b, exhibited a nonlinear dependence on mass flow rate. Effectiveness decreased as the flow rate increased from 0.03 to 0.04 kg·s^{-1} but recovered at 0.05 kg·s^{-1}. This behavior arises from a shift in the limiting heat capacity rate between the hot and cold streams, which modifies the maximum attainable heat transfer and alters the relative contributions of fluid- and solid-side thermal resistances.

Hot-side pressure drops, shown in Figure 5c, increased nearly linearly with mass flow rate, reaching 1586.6 Pa at 0.05 kg·s^{-1} and 100°C. This trend results from higher flow velocities, increased Reynolds numbers, and greater form drag across the fin surfaces. Inlet temperature also influences the pressure drop: higher temperatures reduce air viscosity, slightly lowering the pressure drop at a given flow rate. The minimum pressure drop of 401.5 Pa occurred at the lowest tested mass flow rate of 0.03 kg·s^{-1} and an inlet temperature of 50°C, reflecting the combined effects of low velocity and high viscosity.

Cold-side pressure drops, shown in Figure 5d, were substantially lower than those on the hot side, remaining within 800–900 Pa. This stability is attributed to the fixed cold-side mass flow rate of 0.04 kg·s^{-1}, which maintains consistent flow velocity and

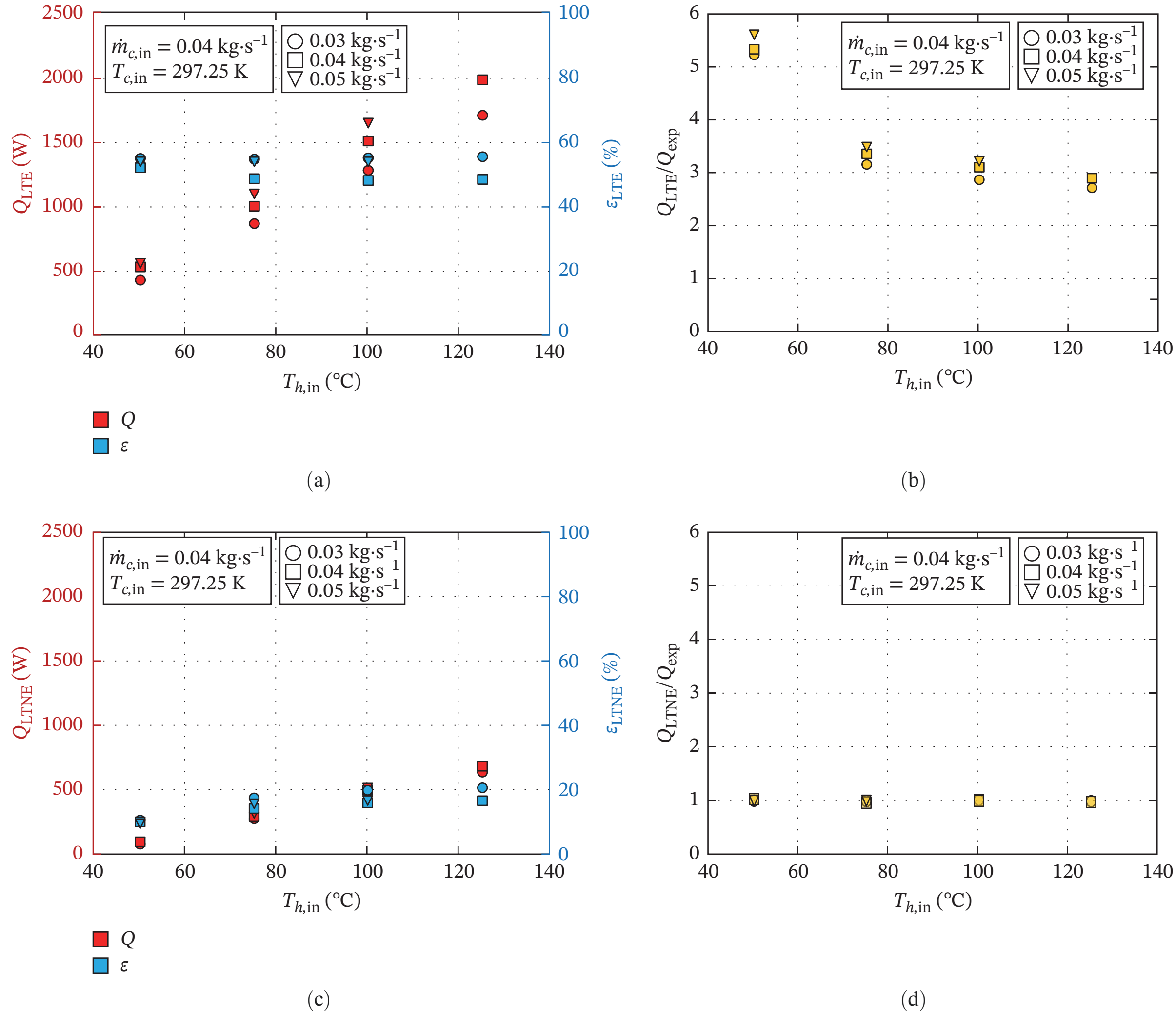

FIGURE 6 | Comparison of predicted and experimental heat transfer performance. (a,c) Predicted heat transfer rate and effectiveness from the LTE and LTNE porous-medium models. (b,d) Ratios of predicted to experimental heat transfer rate (Q_{model}/Q_{exp}). LTNE predictions agree with experimental results within 5%, whereas LTE overpredicts by factors of 2.7–5.6.

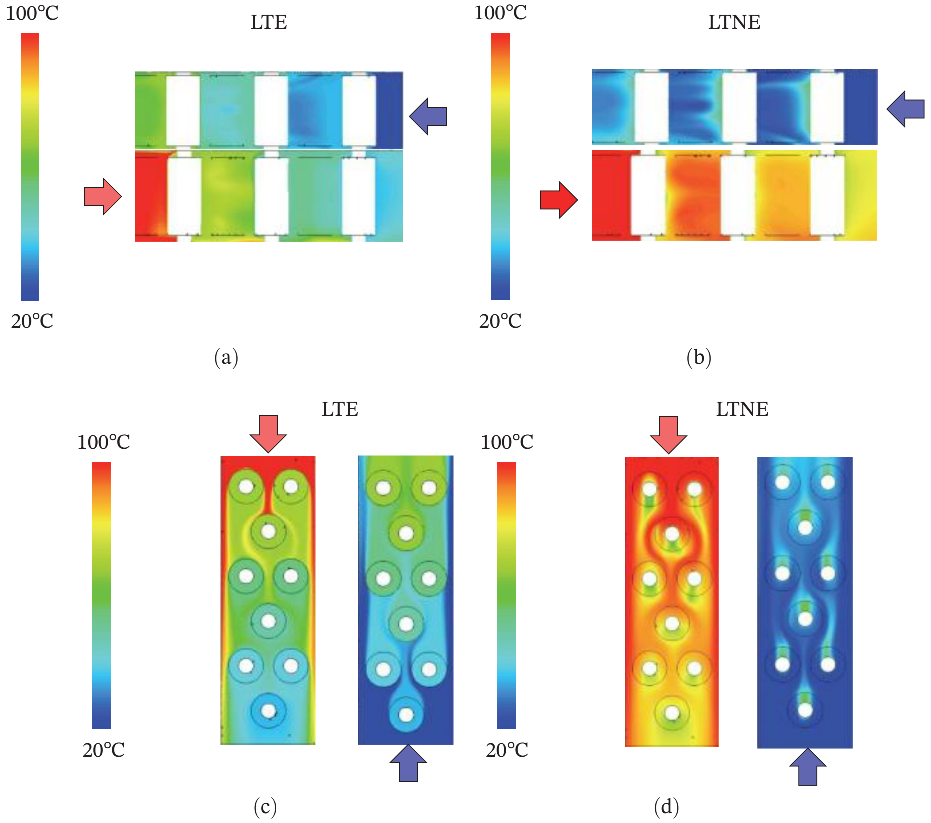

FIGURE 7 | Temperature contours and wake structures predicted by LTE and LTNE models. (a,b) Side views. (c,d) Top views. The LTE model produces unrealistic inlet gradients and fails to resolve vortex-induced wakes, whereas the LTNE model accurately captures wake structures and downstream temperature distributions.

hydraulic resistance regardless of variations in hot-side operating conditions.

To further evaluate the reliability of the experimental trends, the propagated uncertainties of the measured parameters were analyzed and are summarized in Table 4.

4.2 | Comparative Analysis of Heat Transfer and Temperature Distribution

Figure 6 compares predicted heat transfer rates and effectiveness obtained from two porous-medium approaches: the LTE model and the LTNE model. Figure 6a,b presents LTE predictions, while Figure 6c,d presents LTNE predictions. In each pair, the left panel shows predicted heat transfer rate and effectiveness, and the right panel displays the ratio of the predicted to experimental heat transfer ($Q_{\text{model}}/Q_{\text{exp}}$).

Figure 6a,b indicates that the LTE model captures the general trend of increasing heat transfer with higher inlet temperatures and mass flow rates. At 0.03 kg·s^{-1}, Q_{LTE} increases from 441.1 W at 50°C to 1722.1 W at 125°C, a rise of ~290%. At a fixed inlet temperature of 50°C, increasing the mass flow rate from 0.03 to 0.05 kg·s^{-1} raises Q_{LTE} by ~31.5%. Despite these qualitative agreements, LTE consistently overpredicts heat transfer, with errors ranging from factors of 2.7–5.6. The largest deviations occur at low temperatures, with an average overprediction exceeding 260% relative to experimental measurements. Furthermore, while experimental data indicate that effectiveness increases with inlet temperature, LTE predicts nearly constant values. This systematic bias results from the LTE assumption of an infinite HTC, which suppresses fluid–solid temperature differences and boundary-layer growth. Consequently, LTE errors exceed the experimental uncertainty in Q_{exp} (6.26%) by more than a factor of four.

Figure 6c,d demonstrates that the LTNE model, which incorporates finite and physically derived interfacial HTCs, overcomes these limitations. Under the same conditions where LTE predicted 441.1–1,722.1 W, LTNE yielded 86.7–644.8 W, closely matching the experimental convective behavior. LTNE also reproduces the observed variation in effectiveness, including the initial decrease as the mass flow rate increases from 0.03 to 0.04 kg·s^{-1} and the subsequent recovery at 0.05 kg·s^{-1}. Across all conditions, the maximum absolute error remained within 2.4 W (<5%), reducing LTE overpredictions from more than 260% to below 5%. These results confirm that LTNE provides reliable predictions, with both Q and ε remaining well within the experimental uncertainty of 6.26%.

Figure 7 presents temperature contours predicted by the LTE and LTNE models. The hot side operated at a mass flow rate of 0.03 kg·s^{-1} with an inlet temperature of 50°C, while the cold side operated at 0.04 kg·s^{-1} with an inlet temperature of 24°C.

The LTE model predicts steep and physically unrealistic temperature gradients near the inlet. This distortion arises from the

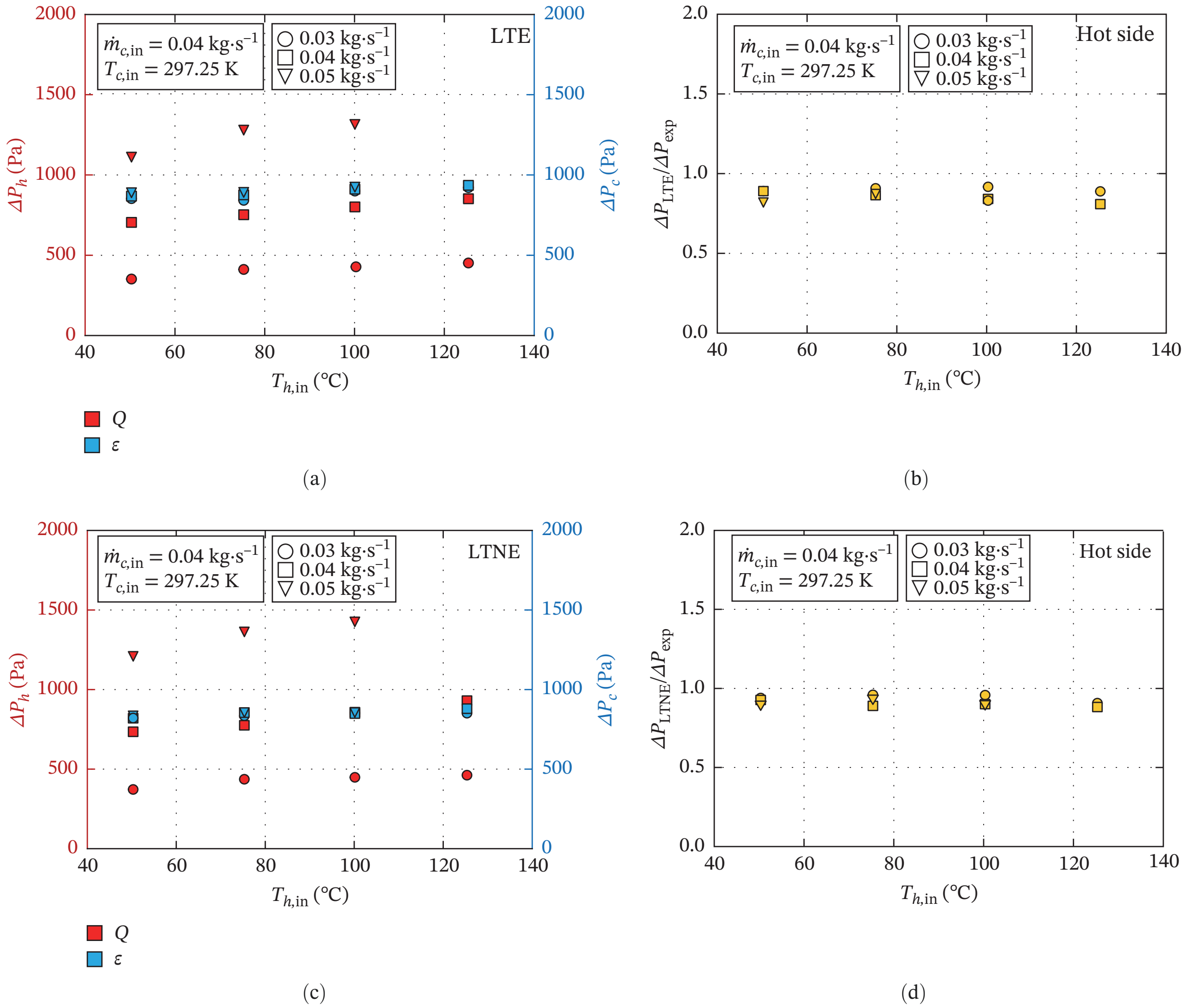

FIGURE 8 | Predicted hot- and cold-side pressure drops and comparison with experiments. (a,c) Predicted hot- and cold-side pressure drops from LTE and LTNE models. (b,d) Ratios of predicted to experimental hot-side pressure drop ($\Delta P_{\mathrm{model}}/\Delta P_{\mathrm{exp}}$). The LTNE model reduces hot-side errors by ~45% and cold-side errors by ~60% compared to LTE.

assumption of an infinitely large HTC, which artificially accelerates thermal diffusion and suppresses the natural development of boundary layers. Further downstream, LTE fails to capture the alternating temperature variations caused by Kármán vortex shedding behind the heat pipes, resulting in smeared gradients and poor wake resolution.

In contrast, the LTNE model incorporates finite, physically derived interfacial HTCs. This approach produces smooth, physically consistent temperature fields along the flow direction. It also resolves the periodic wake patterns and associated thermal gradients downstream of the heat pipes with high clarity, providing a marked improvement over the LTE model.

4.3 | Comparative Evaluation of Pressure Drops

Figure 8 compares hot- and cold-side pressure drops predicted by the LTE and LTNE porous-medium models. Panels a and b present LTE results, while panels c and d present LTNE results. In each pair, the left panel shows the predicted pressure drops and the right panel displays the ratio of predicted to experimental hot-side pressure drop ($\Delta P_{\mathrm{model}}/\Delta P_{\mathrm{exp}}$).

Figure 8a,b illustrates LTE predictions. Hot-side pressure drop increases nearly linearly with mass flow rate, reaching its maximum at 0.05 kg·s^{-1} and 100°C. Compared with experimental measurements, ΔP_{LTE} is underpredicted by 8.4%–16.6%, which is two to five times greater than the experimental uncertainty. Under the same inlet conditions, LTE predicts lower hot-side values than LTNE because lower average air temperatures reduce viscosity. On the cold side, LTE predicts slightly higher pressure drops, as the assumption of infinite HTCs enhances heat exchange, raising air temperature and viscosity. Cold-side deviations from experiments range from 2.5% to 12.5%. Across all conditions, the cold-side pressure drop remains nearly constant with variations in hot-side flow rate, consistent with the measurement repeatability.

Figure 8c,d shows LTNE predictions. Hot-side pressure drops also increase linearly with mass flow rate, but deviations from experiments are smaller, ranging from 3.4% to 10.6%. Cold-side

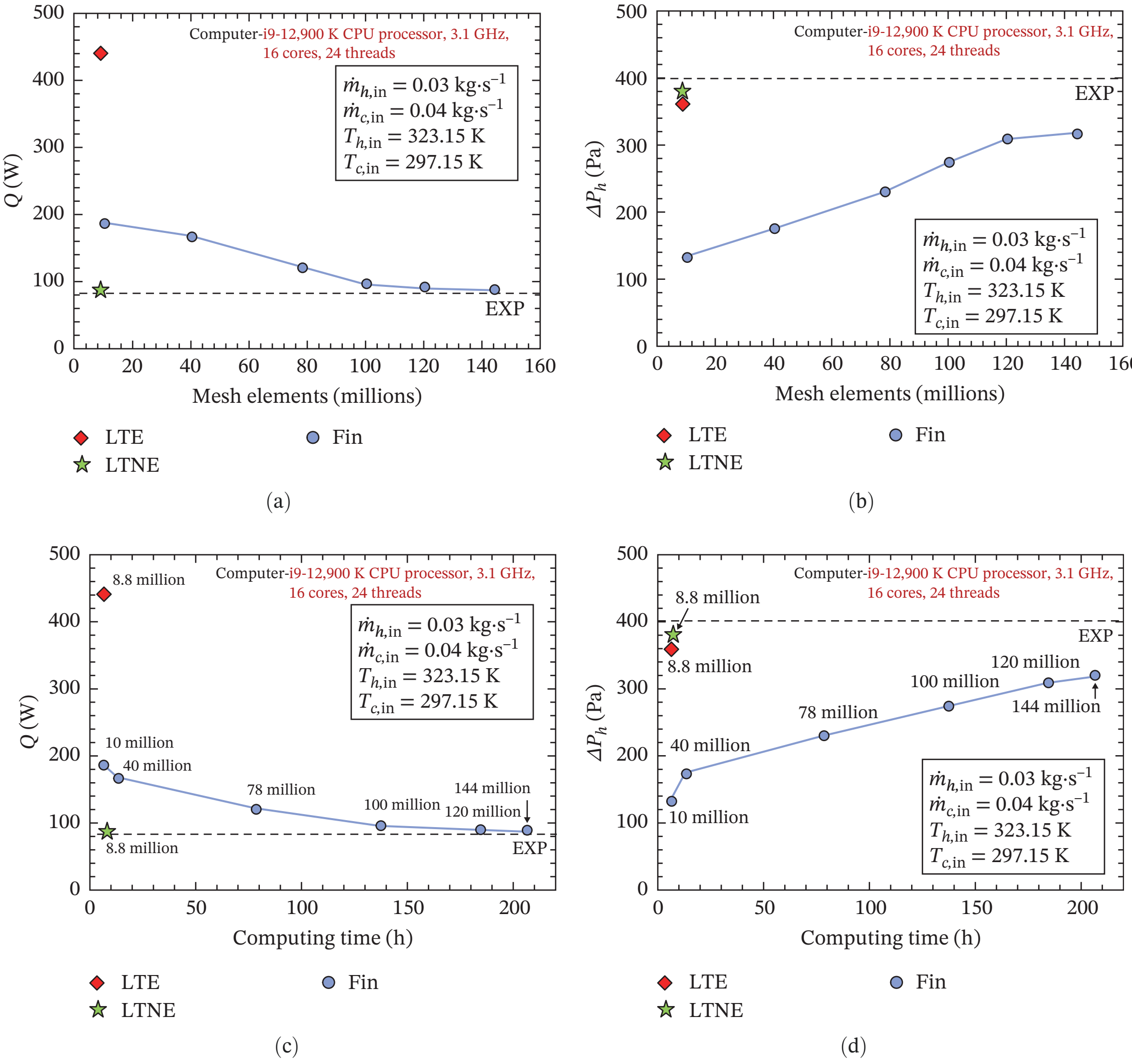

FIGURE 9 | Impact of mesh density and computation time on model accuracy. (a) Deviations in predicted heat transfer rate with increasing mesh element count. (b) Deviations in predicted pressure drop with increasing mesh element count. (c) Errors in predicted heat transfer rate as a function of computation time. (d) Errors in predicted pressure drop as a function of computation time. The LTNE model achieves the accuracy of the highest-density fin-resolved model while reducing computation time by ~97%, whereas the LTE model exhibits large discrepancies in heat transfer predictions.

differences fall within 0.3%–4%. Compared with LTE, LTNE reduces the average hot-side error by ~45% and the cold-side error by over 60%. These improvements exceed the experimental uncertainty, confirming systematic gains in predictive accuracy. The enhanced performance arises from LTNE's incorporation of finite, physically derived interfacial HTCs, which more accurately capture the coupling between thermal and viscous effects in both flow paths.

4.4 | Comparative Assessment of Accuracy and Computational Efficiency in LTEL, LLTNE, and Fin-Resolved Models

This section evaluates the trade-off between predictive accuracy and computational cost for three modeling strategies: the LTE porous-medium model, the LTNE porous-medium model, and the fin-resolved geometry model. The analysis quantifies the influence of mesh density and computation time on prediction accuracy to identify the most efficient approach for simulating compact finned heat exchangers. All simulations were conducted under fixed operating conditions: hot-side mass flow rate of 0.03 kg·s^{-1} at 50°C and cold-side mass flow rate of 0.04 kg·s^{-1} at 24°C, using a workstation equipped with an Intel i9-12900K CPU (3.1 GHz, 16 cores, 24 threads).

Figure 9a,b illustrates the effect of mesh density on prediction errors for heat transfer rate and pressure drop. The porous-medium models employed a constant mesh of 8.8 million elements. In contrast, the fin-resolved model required between 10 million and 144 million elements to achieve convergence. At 10 million elements, errors were 123% (188 W) for heat transfer and 66% (134 Pa) for pressure drop, with a computation time of ~6 h. Increasing the mesh to 40 million elements reduced errors to 100.2% for heat transfer and 56% for pressure drop, while computation time increased to 13 h. At the highest resolution of 144 million elements, errors decreased to 3.75% for heat transfer and 20% for pressure drop, but computation time increased to 206 h.

TABLE 4 | Uncertainty analysis of the experiment.

Hot-side inlet temperature (°C)	Hot-side flow rate (kg/s)	Heat transfer rate (%)	Effectiveness (%)	*P* (Pa)
50	0.03	11.47	8.15	2.03
	0.04	9.92	8.83	2.03
	0.05	10.69	9.06	2.03
75	0.03	6.55	2.56	2.03
	0.04	5.3	3.03	2.03
	0.05	4.93	2.86	2.03
100	0.03	6.11	1.56	2.03
	0.04	4.66	1.9	2.03
	0.05	4.14	1.79	2.03
125	0.03	5.88	1.1	2.03
	0.04	4.42	1.35	2.03

Figure 9c,d highlights the influence of computation time on predictive accuracy. At 8.8 million elements, LTE exhibited a pressure drop error of 10.2% and a heat transfer error of 424.8%, the latter caused by its assumption of an infinite HTC. Under the same mesh, LTNE achieved significantly improved accuracy, with errors of 3.17% for heat transfer and 5.2% for pressure drop. This corresponds to a reduction of over 99% in heat transfer error and ~50% in pressure drop error relative to LTE, both well within the experimental uncertainty.

Overall, LTNE reproduces the accuracy of the highest-resolution fin-resolved model while reducing computation time by ~97%, establishing it as the most effective and practical option for large-scale simulations of compact finned heat exchangers.

5 | Conclusion

This study developed a porous-medium modeling framework for compact HPHXs by integrating anisotropic flow resistance coefficients with an LTNE formulation. The framework was validated against detailed experimental measurements and benchmarked against both an LTE porous-medium model and a fully resolved fin-geometry model.

The LTNE model accurately predicted heat transfer, effectiveness, and pressure drop, maintaining errors within 5% for thermal performance and 5.2% for hydraulic performance across all tested conditions. Compared with LTE, LTNE reduced average hot-side and cold-side pressure drop deviations by ~45% and 60%, respectively, and eliminated the systematic overprediction of heat transfer. Its predictive accuracy matched that of the highest-resolution fin-resolved model while reducing computational time by ~97%, enabling reliable simulations without the prohibitive cost of fully resolved models.

These results demonstrate that the LTNE porous-medium framework is a robust and computationally efficient tool for the design and optimization of compact finned heat exchangers. Future work will extend this approach to transient operating regimes, incorporate advanced turbulence and phase-change models, and integrate optimization algorithms to enable the automated and high-fidelity design of next-generation compact heat recovery systems.

Nomenclature

A:	Area (mm^2)
a:	Fitting coefficient
b:	Fitting coefficient
C:	Heat capacity rate ($W{\cdot}K^{-1}$)
C_1:	Viscous resistance coefficient
C_2:	Inertial resistance coefficient
C_{ij}:	Inertial loss coefficient matrix
c_p:	Specific heat ($J{\cdot}kg^{-1}{\cdot}K^{-1}$)
D_o:	Heat pipe outer diameter (mm)
D_{ij}:	Viscous loss coefficient matrix
H:	Height (mm)
HTC:	Heat transfer coefficient ($W{\cdot}m^{-2}{\cdot}K^{-1}$)
h:	Hour
k:	Thermal conductivity ($W{\cdot}m^{-1}{\cdot}K^{-1}$)
Δn:	Porous-media thickness (m)
L:	Length (mm)
$\dot{m}$:	Mass flow rate ($kg{\cdot}s^{-1}$)
Q:	Heat transfer rate (W)
Re:	Reynolds number
S_i:	Momentum source term in the i^{th} direction ($kg{\cdot}m^{-2}{\cdot}s^{-2}$)
T:	Temperature (°C)
t:	Thickness (mm)
u:	Fluid velocity ($m{\cdot}s^{-1}$)
W:	Width (mm)

Greek Symbols

Δ:	Difference
α:	Permeability (m^2)
ε:	Effectiveness
μ:	Dynamic viscosity ($kg \cdot m^{-1} \cdot s^{-1}$)
ρ:	Density ($kg \cdot m^{-3}$)

Subscripts

air:	Air
c:	Cold
eff:	Effective
h:	Hot
in:	Inlet
max:	Maximum
min:	Minimum
out:	Outlet
wall:	Wall.

Acknowledgments

This work was supported by the International Cooperative R&D Program of the Korea Institute of Energy Technology Evaluation and Planning (KETEP), a grant funded by the Ministry of Trade, Industry & Energy, Korea (Grant RS-2024-00436521 and 20212020800270), and the Chung-Ang University Graduate Research Scholarship in 2024.

Funding

This study was funded by Korea Institute of Energy Technology Evaluation and Planning, (Grant RS-2024-00436521 and 20212020800270) and Chung-Ang University.

Conflicts of Interest

The authors declare no conflicts of interest.

Data Availability Statement

The data that support the findings of this study are available from the corresponding author upon reasonable request.

References

1. A. Mahmoudi, M. Fazli, and M. R. Morad, “A Recent Review of Waste Heat Recovery by Organic Rankine Cycle,” *Applied Thermal Engineering* 143 (2018): 660–675.

2. H. Ritchie, P. Rosado, and M. Roser, “CO_2 and Greenhouse Gas Emissions,” (Our World in Data (2023).

3. C. Forman, I. K. Muritala, R. Pardemann, and B. Meyer, “Estimating the Global Waste Heat Potential,” *Renewable and Sustainable Energy Reviews* 57 (2016): 1568–1579.

4. W. Srimuang and P. Amatachaya, “A Review of the Applications of Heat Pipe Heat Exchangers for Heat Recovery,” *Renewable and Sustainable Energy Reviews* 16, no. 6 (2012): 4303–4315.

5. G. Geum, S. Kang, S. Cho, et al., “Thermal Performance Analysis of Heat Pipe Heat Exchanger for Effective Waste Heat Recovery,” *International Communications in Heat and Mass Transfer* 151 (2024): 107223.

6. X. P. Wu, P. Johnson, and A. Akbarzadeh, “Application of Heat Pipe Heat Exchangers to Humidity Control in Air-Conditioning Systems,” *Applied Thermal Engineering* 17, no. 6 (1997): 561–568.

7. S. H. Noie-Baghban and G. R. Majideian, “Waste Heat Recovery Using Heat Pipe Heat Exchanger (HPHE) for Surgery Rooms in Hospitals,” *Applied Thermal Engineering* 20, no. 14 (2000): 1271–1282.

8. M. A. Abd El-Baky and M. M. Mohamed, “Heat Pipe Heat Exchanger for Heat Recovery in Air Conditioning,” *Applied Thermal Engineering* 27, no. 4 (2007): 795–801.

9. M. Ahmadzadehtalatapeh and Y. H. Yau, “The Application of Heat Pipe Heat Exchangers to Improve the Air Quality and Reduce the Energy Consumption of the Air Conditioning System in a Hospital Ward—A Full Year Model Simulation,” *Energy and Buildings* 43, no. 9 (2011): 2344–2355.

10. H. Jouhara, S. Almahmoud, A. Chauhan, et al., “Experimental and Theoretical Investigation of a Flat Heat Pipe Heat Exchanger for Waste Heat Recovery in the Steel Industry,” *Energy* 141 (2017): 1928–1939.

11. H. Jouhara, D. Bertrand, B. Axcell, et al., “Investigation on a Full-Scale Heat Pipe Heat Exchanger in the Ceramics Industry for Waste Heat Recovery,” *Energy* 223 (2021): 120037.

12. J. Zhang, T. Li, Z. Shen, et al., “Investigations of Multiphysics Models on a Megawatt-Level Heat Pipe Nuclear Reactor Based on High-Fidelity Approaches,” *Nuclear Science and Engineering* 198, no. 5 (2024): 1097–1121.

13. Y. Qian, T. Liu, Y. Zhang, et al., “Evaluation of Load Following Control Strategy for Heat Pipe-Cooled Microreactor Coupled With Closed Brayton Cycle System,” *Progress in Nuclear Energy* 185 (2025): 105768.

14. S. U. Khalid, S. Hasnain, H. M. Ali, S. Bano, M. A. Nasir, and N. Abbas, “Experimental Investigation of Aluminum Fins on Relative Thermal Performance of Sintered Copper Wicked and Grooved Heat Pipes,” *Progress in Nuclear Energy* 152 (2022): 104374.

15. A. Shahsavar, M. A. Bakhshizadeh, and H. M. Ali, “Comprehensive Evaluation of the Entropy Generation in Oval Twisted Double-Pipe Heat Exchanger Using Non-Newtonian Nanofluid Using Two-Phase Mixture Model,” *Engineering Analysis With Boundary Elements* 152 (2023): 637–644.

16. S. Lee, S. Kang, Y. Kim, et al., “Thermal Design Framework of Heat Pipe Heat Exchanger for Efficient Waste Heat Recovery,” *Energy* 318 (2025): 134731.

17. I. Yilgor, Z. D. Sellers, J. L. Hartvigsen, et al., “Recent Developments and Findings of Heat Pipe Experiments for Microreactor Applications,” *Nuclear Technology* 211, no. 5 (2025): 905–939.

18. B. Selma, M. Désilets, and P. Proulx, “Optimization of an Industrial Heat Exchanger Using an Open-Source CFD Code,” *Applied Thermal Engineering* 69, no. 1-2 (2014): 241–250.

19. D. Brough, J. Ramos, B. Delpech, and H. Jouhara, “Development and Validation of a TRNSYS Type to Simulate Heat Pipe Heat Exchangers in Transient Applications of Waste Heat Recovery,” *International Journal of Thermofluids* 9 (2021): 100056.

20. J. Ramos, A. Chong, and H. Jouhara, “Experimental and Numerical Investigation of a Cross Flow Air-to-Water Heat Pipe-Based Heat Exchanger Used in Waste Heat Recovery,” *International Journal of Heat and Mass Transfer* 102 (2016): 1267–1281.

21. K. Lindqvist and E. Næss, “A Validated CFD Model of Plain and Serrated Fin-Tube Bundles,” *Applied Thermal Engineering* 143 (2018): 72–79.

22. F. Ejaz, N. A. A. Qasem, S. Z. Shuja, H. M. Ali, and S. M. Zubair, “Impact of Pin-Fin Shape on Thermal-Hydraulic Performance Under Condensation of Flat-Tube Heat Exchangers: Numerical and Machine Learning Approaches,” *Applied Thermal Engineering* 286 (2026): 129315.

23. W. Wang, J. Guo, S. Zhang, J. Yang, X. Ding, and X. Zhan, "Numerical Study on Hydrodynamic Characteristics of Plate-Fin Heat Exchanger Using Porous Media Approach," *Computers & Chemical Engineering* 61 (2014): 30–37.

24. G. Amhalhel and P. Furmanski, "Problems of Modeling Flow and Heat Transfer in Porous Media," *Journal of Power Technologies* 85 (1997): 55.

25. A. M. Hayes, J. A. Khan, A. H. Shaaban, and I. G. Spearing, "The Thermal Modeling of a Matrix Heat Exchanger Using a Porous Medium and the Thermal Non-Equilibrium Model," *International Journal of Thermal Sciences* 47, no. 10 (2008): 1306–1315.

26. P. Gangapatnam, R. Kurian, and S. P. Venkateshan, "Numerical Simulation of Heat Transfer in Metal Foams," *Heat and Mass Transfer* 54, no. 2 (2018): 553–562.

27. D. Seo, J. Park, J. Shim, et al., "Enhancing Heat Transfer Performance of a Two-Phase Closed Thermosyphon Using a Polymer-Coated Hydrophobic Condenser," *Applied Thermal Engineering* 196 (2021): 117350.

28. H. Martin, "The Generalized Lévêque Equation and Its Practical Use for the Prediction of Heat and Mass Transfer Rates From Pressure Drop," *Chemical Engineering Science* 57, no. 16 (2002): 3217–3223.

29. A. Ganguli and S. B. Yilmaz, "New Heat Transfer and Pressure Drop Correlations for Crossflow Over Low-Finned Tube Banks," *Heat Transfer: Pittsburgh 1987* (1987): 9–14.

30. Joint Committee for Guides in Metrology (JCGM), "Guide to the Expression of Uncertainty in Measurement," (International Organization for Standardization (ISO)2008, ISO 50 http://www.bipm.org/en/publications/guides/gum.html.

31. Y. Kim, D. H. Shin, J. S. Kim, S. M. You, and J. Lee, "Boiling and Condensation Heat Transfer of Inclined Two-Phase Closed Thermosyphon With Various Filling Ratios," *Applied Thermal Engineering* 145 (2018): 328–342.

32. Z.-Z. Li, Y.-D. Ding, Q. Liao, M. Cheng, and X. Zhu, "An Approach Based on the Porous Media Model for Numerical Simulation of 3D Finned-Tubes Heat Exchanger," *International Journal of Heat and Mass Transfer* 173 (2021): 121226.

Supporting Information

Additional supporting information can be found online in the Supporting Information section. (*Supporting Information*)

Supporting Information is available from the Wiley Online Library or from the author. Section I: Results of uncertainty analysis. Table S1: Summary of uncertainty analysis for heat transfer rate and effectiveness. Section II: Computational governing equations. Section III: Grid-independence test. Figure S1: Computational grid. (a) Mesh-independence test result. (b) Image showing the inflation mesh. Section IV: Unit-cell simulation. Figure S2: Unit-cell simulations for coefficient characterization in the porous-medium model. (a) Computational domain and boundary conditions for resistance coefficients. (b) Computational domain and boundary conditions for HTCs.